Mechanistic Insights into Methane Total Oxidation over Cu/Hydroxyapatite Catalyst Synthesized with β-Cyclodextrin Assistance

Reza Monjezi, Alexandra Bouriakova, Ana Bjelić, Philippe Heynderickx, Geraldine Heynderickx, Dirk Poelman, Jean-Marc Giraudon, Jean-François Lamonier, Rino Morent, Joris Thybaut

Mechanistic Insights into Methane Total Oxidation over Cu/Hydroxyapatite Catalyst Synthesized with β-Cyclodextrin Assistance

Reza Monjezi[1], Alexandra Bouriakova[1], Ana Bjelić[1], Philippe M. Heynderickx[2,3], Geraldine J. Heynderickx[1], Dirk Poelman[4], Jean-Marc Giraudon[5], Jean-François Lamonier[5], Rino Morent[6], Joris W. Thybaut[1*]

[1]*Laboratory for Chemical Technology, Ghent University, Technologiepark 125, B-9052 Ghent, Belgium*

[2]*Ghent University Global Campus, 119-5 Songdomunhwa-Ro, Yeonsu-Gu Songdo Incheon 406-840, South Korea*

[3]*Department Green Chemistry and Technology, Ghent University, Coupure Links 653, 9000 Ghent, Belgium*

[4]*LumiLab, Department of Solid State Sciences, Ghent University, Krijgslaan 281-S1, Ghent, B-9000, Belgium*

[5]*Univ. Lille, CNRS, Centrale Lille, Univ. Artois, UMR 8181, UCCS, Unité de Catalyse et Chimie du Solide, Lille F-59000, France*

[6]*Research Unit Plasma Technology, Ghent University, St-Pietersnieuwstraat 41, 9000 Ghent, Belgium*

* *Joris.Thybaut@UGent.be*

Abstract

The total oxidation of methane (CH_4), a highly stable alkane volatile organic compound (VOC), using low-cost Cu-based catalysts, has garnered considerable attention. Nonetheless, challenges such as Cu particle agglomeration and the lack of consensus on mechanism of CH_4 total oxidation over Cu-based catalysts remain. In this work, β-cyclodextrin (βCD) was introduced during Cu/hydroxyapatite catalyst (βCD-Cu/HAP) preparation, and its catalytic performance in CH_4 total oxidation was compared with the Cu/HAP catalyst. Both materials were prepared using the wet impregnation method and thoroughly characterized. It was found that utilization of βCD, which decomposed during calcination, led to smaller Cu particle size (from 61 to 34 nm) and better Cu dispersion (from 1.9 to 3.5%), resulting in an enhancement of the catalyst reduction properties. Additionally, the βCD-Cu/HAP catalyst possessed a higher oxygen storage capacity, demonstrating its superior ability to replenish the oxygen vacancies. The βCD-Cu/HAP catalyst activity was double that of the original Cu/HAP catalyst with a 20 kJ mol^{-1} lower activation energy, as determined by fitting the initial reaction rate to a power-law model. Further, Langmuir–Hinshelwood (LH), Eley–Rideal (ER), and Mars–van Krevelen (MVK) type rate expressions were regressed to the experimental data. After statistical and physico-chemical assessments, the MVK mechanism involving two oxidized sites and one reduced site with H_2O adsorption on oxidized sites was identified as the most appropriate model for describing the experimental data. These findings offer an enhanced understanding of CH_4 total oxidation, guiding the development of efficient, low-cost catalysts for this reaction.

Environmental Implication

Volatile organic compounds (VOCs) pose significant environmental and health issues due to their toxicity and widespread sources. Among VOCs, alkane contribute to a large proportion

of the VOCs emitted, with light alkanes being particularly challenging to mitigate due to their high stability. Methane, the most stable light alkanes, is the focus of this study. Catalytic oxidation technology offers a promising solution for VOC mitigation. In our work, we conducted a mechanistic investigation of methane total oxidation, aiming at deepening our understanding of catalytic oxidation of light alkanes, thereby contributing to substantial environmental benefits.

Keywords

catalytic oxidation; volatile organic compounds; β-cyclodextrin; copper; Mars–van Krevelen

53 Nomenclature

Roman symbols

d_p	Mean pore diameter (nm)
d_{crys}	Mean crystallite size (nm)
d_{Cu}	Mean Cu particle size (nm)
D_{Cu}	Copper dispersion (%)
E_a	Activation energy (kJ mol^{-1})
k_{CH_4}	Reduction rate coefficient ($mol_{CH_4} kg_{cat}^{-1} s^{-1} kPa^{-1}$)
k_{O_2}	Reoxidation rate coefficient ($mol_{O_2} kg_{cat}^{-1} s^{-1} kPa^{-1}$)
k_r	Reaction rate coefficient ($mol_{CH_4} kg_{cat}^{-1} s^{-1}$)
k_0	Pre-exponential factor ($mol_{CH_4} kg_{cat}^{-1} s^{-1}$)
$k_{0,app}$	Apparent pre-exponential factor (mol kg_{cat}^{-1} $s^{-1}(kPa)^{-1+(m+n)}$)
m	Apparent CH_4 reaction order, (-)
n	Apparent O_2 reaction order, (-)
p_i	Partial pressure of component i (kPa)
p_{loop}	Loop pressure (kPa)
R	Universal gas constant (kJ $mol^{-1}K^{-1}$)
S_{BET}	BET surface area ($m^2 g_{cat}^{-1}$)
TOF_0	Initial turnover frequency ($mol_{CH_4} mol_O^{-1} s^{-1}$)
V_p	Specific pore volume ($cm^3 g_{cat}^{-1}$)
W_{cat}	Catalyst weight (kg_{cat})
X_{CH_4}	CH_4 conversion ($mol_{CH_4} mol_{CH_4,0}^{-1}$)
y_{Cu}	Cu content of the catalyst determined from ICP-OES data (wt %)

Greek symbols

$\Delta S'_{ads}$	Replacement of adsorption entropy (J $mol^{-1}K^{-1}$)
ΔS_{ads}	Adsorption entropy (J $mol^{-1}K^{-1}$)

Abbreviations and acronyms

BET	Brunauer–Emmett–Teller
BIC	Bayesian Information Criterion
ER	Eley-Rideal
HAP	Hydroxyapatite
H_2-TPR	Hydrogen Temperature-Programmed Reduction
ICP-OES	Inductively Coupled Plasma-Optical Emission Spectrometry
LH	Langmuir-Hinshelwood
MVK	Mars-van Krevelen
OSC	Oxygen Storage Capacity
PL	Power-Law
RDS	Rate-Determining Step
TCD	Thermal Conductivity Detector
VOC	Volatile Organic Compound
XPS	X-ray Photoelectron Spectroscopy
XRD	X-Ray Diffraction
βCD	β-Cyclodextrin

54

1. Introduction

The ever-growing industrialization and urbanization are raising emissions of volatile organic compounds (VOCs), i.e., carbon-based chemicals with boiling points below 250 °C. VOCs lead to a decrease in air quality, being the source of severe hazards, such as the formation of photochemical smog and a diversity of adverse health issues [1]. VOC emissions can be controlled by a variety of methods. Among these, catalytic oxidation stands out as an economically viable technology for the abatement of VOC pollutants [2–4].

Among VOCs, methane (CH_4), mainly emitted from industry and agriculture sectors, is one of the most abundant in the atmosphere [5,6]. As a prototypical light alkane, CH_4 is notably stable due to its symmetric tetrahedral structure, featuring four equivalent C-H bonds [7]. This high stability poses significant challenges for its complete elimination. Consequently, the CH_4 total oxidation has been widely used as a method to effectively mitigate its presence in the atmosphere [8–10].

Cu-based catalysts have demonstrated high activity in VOC total oxidation, including CH_4 total oxidation [11–13]. However, these catalysts suffer from agglomeration of CuO particles, resulting in the formation of bulk CuO particles at high Cu content [11,14,15]. Recently, cyclodextrins have emerged as promising agents in catalyst preparation, particularly for their role in enhancing metal dispersion [16–21]. Bai et al. [18] demonstrated that β-cyclodextrin (βCD) addition during synthesis of Co_3O_4/ZrO_2 catalysts for formaldehyde oxidation significantly improved dispersion, resulting in smaller and more reducible Co_3O_4 particles, thereby boosting catalytic performance. Other works focusing on Cu-based catalysts have also reported a similar effect of βCD on the dispersion of Cu atoms [20,21].

Among the various support materials investigated [22], hydroxyapatite ($Ca_{10}(PO_4)_6(OH)_2$, HAP), has recently received increasing interest [20,23–26] due to its low cost, non-toxicity,

thermal and chemical stability, and its ability to undergo ion exchanges. Moreover, the HAP structure features accessible surface Ca^{2+} sites that facilitate the cation exchange process [24], enabling metal ions, such as Cu, to be located on the surface. These intrinsic features position HAP as a promising support material for total oxidation reactions, including oxidation of CH_4 [27,28].

Kinetic models play a vital role in elucidating reaction mechanisms, offering valuable insights into catalyst development, and serving as effective tools for predicting and optimizing chemical processes. Langmuir-Hinshelwood (LH), Eley-Rideal (ER), and Mars-van Krevelen (MVK) mechanisms have been proposed as possible mechanisms for CH_4 total oxidation [29]. Despite the extensive research conducted on the CH_4 total oxidation over Cu-based catalysts [11,12,30–32], only a limited number of studies have focused on elucidating the reaction mechanism. In addition, the current literature lacks unanimity regarding the mechanism for CH_4 total oxidation over Cu-based catalysts. To the best of our knowledge, only two research studies have specifically investigated the CH_4 total oxidation mechanism over Cu-based catalysts, revealing that CH_4 oxidation follows MVK and ER mechanisms over CuO nanowires [31] and Cu/γ-Al_2O_3 [32], respectively. Considering the limited research and lack of consensus, a systematic kinetic study is required to comprehensively elucidate the reaction mechanism of CH_4 total oxidation reaction over Cu-based catalysts.

This work is driven by two primary objectives. First, it investigates the influence of βCD addition during the synthesis of Cu/HAP catalyst on its ultimate properties and catalytic performance in CH_4 total oxidation. Second, it aims to develop and validate a comprehensive kinetic model along with its corresponding elementary steps that accurately describes the CH_4 total oxidation experimental data over Cu-based catalysts. To achieve these objectives, two Cu/HAP catalysts were prepared, one without (the original catalyst) and the other with βCD

addition during synthesis (the modified catalyst). Subsequently, a detailed catalyst characterization and an extensive experimental investigation were conducted on both catalysts. The characterization and catalytic results of both catalysts were compared to unravel the impact of βCD addition during synthesis on the properties and performance of the modified catalyst. Subsequently, kinetic models according to the LH, ER, and MVK reaction mechanisms were regressed to the experimental observations. Finally, a kinetic analysis in conjunction with a thorough interpretation of catalyst characterization results was performed to unveil the underlying mechanism governing CH_4 total oxidation over the modified catalyst. This elucidation not only contributes to bridging the existing knowledge gap but also facilitates the development of more efficient catalyst designs for CH_4 total oxidation, addressing both environmental concerns and industrial needs.

2. Procedures

2.1. Catalyst Synthesis

HAP support with a theoretical molar Ca/P ratio of 1.67 was prepared by the co-precipitation method. Then, two Cu-containing catalysts, with and without βCD addition during synthesis, were prepared by wet impregnation method targeting a theoretical Cu content of 10 wt%. The catalysts were labeled as Cu/HAP and βCD-Cu/HAP, with the latter indicating the incorporation of βCD during synthesis. It is important to clarify that the βCD mentioned in the catalyst name does not imply its presence in the calcined catalysts, as it decomposes during the calcination treatment. The related procedures are described in detail in the Supporting Information (SI), S2.1.

2.2. Catalyst Characterization

HAP support and Cu-containing catalysts were thoroughly characterized. Inductively Coupled Plasma-Optical Emission Spectrometry (ICP-OES) was employed to quantify the elemental

composition (y_{Cu}), verifying metal content in accordance with intended (experimental) values. N_2-adsorption experiments were conducted to determine the BET surface area (S_{BET}), specific pore volume (V_p) and mean pore diameter (d_p), offering insights into the textural properties of the materials. X-Ray Diffraction (XRD) was used to identify the crystalline phases and determine the crystallite size (d_{crys}), essential for understanding the structural aspects that impact on catalytic activity. N_2O chemisorption allowed for quantifying the Cu dispersion (D_{Cu}) and mean Cu particle size (d_{Cu}), providing quantitative data on the active surface area available for reactions. The nature, reducibility, and quantity of Cu species were assessed by hydrogen Temperature-Programmed Reduction (H_2-TPR), thereby enriching our comprehension of the diverse Cu species present in the catalyst. The oxygen storage capacity (OSC), indicative of active site concentration, was measured using the oxygen pulse chemisorption technique. Lastly, X-ray Photoelectron Spectroscopy (XPS) was performed to obtain the surface composition and oxidation state of components, which is pivotal for understanding surface chemistry and its role in the performance of catalysts. Detailed descriptions of these methods are available in the SI (S2.2.).

2.3. Catalytic Activity

Catalytic testing was performed in a high-throughput setup [33] consisting of 4 parallel stainless steel fixed-bed reactors. The selected operating conditions, see

Table *1*, catalyst pellet diameter and reactor dimensions, led to the acquisition of intrinsic kinetics data [34] (see Table S6). Molar carbon balances were closed within 5% for all experiments, underscoring the reliability of the experimental data. The related experimental details, as well as a schematic diagram of the setup, are provided in SI (S2.3., Figure S1).

The activity of the Cu/HAP and βCD-Cu/HAP catalysts was compared using initial turnover frequency (TOF_0) metric, which is defined as the ratio of the initial reaction rate to the

concentration of active sites (C_O). It is assumed that the concentration of active sites is at least directly proportional, if not equal, to C_O [35]. The equation and derivation of TOF_0 are presented in SI (S2.5.1., see Eq. (S24)).

Table 1: Experimental conditions used for total oxidation of CH_4 over Cu-containing catalysts. N_2 was used as the balance gas.

parameter	unit	value
F_{tot}	/ mol s^{-1}	6.4×10^{-5}
P_{tot}	/ kPa	500
$\frac{W_{cat}}{F_{CH_4,0}}$	/ kg s mol^{-1}	150 – 550
T	/ °C	350 – 450
$p_{CH_4,0}$	/ kPa	2.9 – 8
$p_{O_2,0}$	/ kPa	16.6 – 48.8

2.4. Elementary-Step Based Kinetic Model Construction

After acquiring kinetic experimental data at systematically varied operating conditions, the next step is to identify the underlying reaction mechanism and the corresponding, most appropriate kinetic model describing experimental observations. In this regard, three potential formalisms, i.e., LH, ER, and MVK, are considered as plausible for CH_4 total oxidation over Cu-based catalysts. The resulting mechanisms are founded on elementary steps, which provide insights into the molecular-level events occurring during reaction. An overview and description of possible elementary steps for all mechanisms are documented in SI (refer to S2.4., and Table S1).

2.5. Model Selection

The process of selecting the most suitable kinetic model for CH_4 total oxidation involves three main steps: preliminary model discrimination, non-isothermal regression, and assessment of models and parameters. The preliminary model discrimination process (detailed in SI; S2.5.1.)

is based on the initial reaction rate analysis, encompassing positive/negative reaction orders along with their corresponding values. Following the exclusion of kinetic models incompatible with experimental data in this initial step, non-isothermal regression (detailed in SI; S2.5.2.) was carried out to determine the kinetic parameters associated with the remaining candidate models. Finally, a thorough statistical and physico-chemical evaluation of the kinetic parameters (detailed in SI; S2.5.3.) was performed. In this step, the global significance of the models and that of the individual parameters were assessed using an F test and a t test, respectively. Additionally, correlation among individual estimated parameters in non-isothermal regression were evaluated using binary correlation coefficients. The activation energy and adsorption parameters (enthalpies and entropies) were compared to reported values and assessed for thermodynamic consistency, respectively, to validate the physico-chemical meaning of these parameters. Furthermore, the Bayesian Information Criterion (BIC) of each model was evaluated, facilitating a quantitative comparison of model adequacy while penalizing unnecessary complexity. Moreover, the partial reaction orders were also compared with those obtained from initial reaction rate analysis. This meticulous selection process enables the confident selection of the most appropriate kinetic model. The final model unveils the underlying mechanism and elementary steps of the reaction, hence, providing a robust and in-depth understanding of the reaction kinetics under the investigated operating conditions.

3. Results and Discussion

This section begins with a comprehensive presentation of the characterization results obtained for the HAP support and the Cu/HAP and βCD-Cu/HAP catalysts. Subsequently, the impact of operating conditions on the catalytic activity of Cu/HAP and βCD-Cu/HAP is investigated. Then, the activity of both catalysts is compared by calculating the TOF_0. Finally,

the results of model discrimination are presented, revealing the identification of the most suitable (best combination of physicochemical meaning and statistical performance) model for accurately representing the kinetic performance of CH_4 total oxidation over the βCD-Cu/HAP catalyst.

3.1. Characterization Results

The results of elemental analysis and N_2-adsorption measurement for the bare HAP support and the Cu/HAP and βCD-Cu/HAP catalysts are presented in Table 2. The Cu content was close to the theoretical one for both Cu-containing catalysts, indicating a successful synthesis procedure. Additionally, there is no significant difference in the textural properties among the Cu/HAP and βCD-Cu/HAP catalysts, indicating that the addition of βCD did not affect these properties, consistent with a previous study [36]. Further details regarding ICP-OES and N_2-adsoption results are provided in Table S3 and S3.1. in SI, respectively.

Table 2: Material properties: Cu content as determined by ICP-OES (y_{Cu}); BET surface area (S_{BET}), specific pore volume (V_p) and mean pore diameter (d_p) as determined via N_2-adsorption; mean CuO crystallite size (d_{crys}) obtained via Eq. (S1); Cu surface area (S_{Cu}), mean Cu^0 particle size (d_{Cu}), and dispersion (D_{Cu}) obtained via N_2O chemisorption using Eqs. (S6), (S7), and (S5), respectively.

Material	y_{Cu}(wt%)	$S_{BET}\ (\mathrm{m^2g^{-1}})$	$V_p\ (\mathrm{cm^3g^{-1}})$	d_p (nm)	d_{crys}(nm)	$S_{Cu}(\mathrm{m^2g_{Cu}^{-1}})$	d_{Cu} (nm)	D_{Cu}(%)
HAP	-	97.0 ± 0.1	0.51	20.8	-	-	-	-
Cu/HAP	11.1	79.7 ± 0.1	0.39	20.5	32	10.9	61.4	1.9
βCD-Cu/HAP	11.5	77.3 ± 0.1	0.38	20.5	13	19.6	34.1	3.5

XRD was employed to determine the crystalline phases present in the calcined catalysts. The diffraction patterns depicted in Figure 1 provide evidence of characteristic diffraction lines corresponding to $Ca_5(PO_4)_3(OH)$ (JCPDS 09-0432), confirming the successful formation of the desired HAP structure in all materials.

The CuO monoclinic phase (JCPDS 00-045-0937) was detected in impregnated samples. The intensity of the prominent CuO reflections at 35.5° ($CuO_{(002)}$) and 38.5° ($CuO_{(111)}$) was

significantly lower in the case of βCD-Cu/HAP compared to Cu/HAP catalyst, suggesting a lower degree of crystallinity or smaller crystallites of the former. Remarkably, the distinct CuO reflection at 48.5° ($CuO_{(-202)}$) was absent in the XRD pattern of βCD-Cu/HAP. This observation implies either a different CuO phase distribution or the presence of crystallite sizes below the XRD detection limit owing to the addition of βCD as part of the synthesis procedure. Furthermore, the CuO mean crystallite size, calculated using the Scherrer equation (vide Eq. (S1)), confirmed that the βCD-Cu/HAP catalyst possessed smaller CuO crystallites compared to Cu/HAP, i.e., 13 nm versus 32 nm.

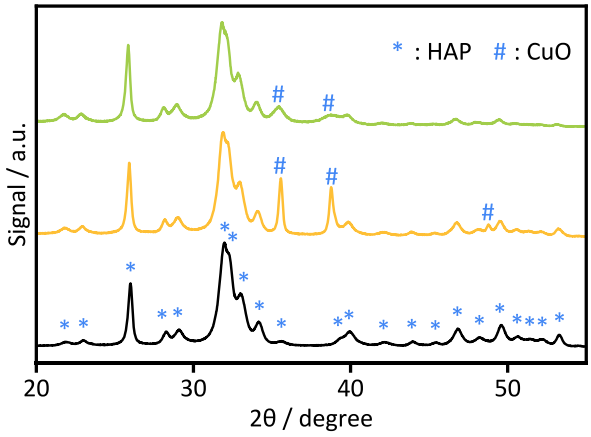

Figure 1: XRD patterns of the HAP ( ), Cu/HAP ( ) and βCD-Cu/HAP ( ).

The N_2O chemisorption findings revealed that the βCD-Cu/HAP catalyst exhibited a higher Cu dispersion and Cu surface area (1.8 times), as well as a smaller mean Cu particle size (34.1 versus 61.4 nm). The enhancement of Cu dispersion and significant reduction in Cu particle size due to the incorporation of βCD during synthesis, have also been observed in previous studies [16,20,21,36]. The N_2O chemisorption results are consistent with XRD results, thereby suggesting that incorporation of βCD hinders Cu agglomeration, leading to the formation of smaller, well-dispersed Cu particles. Notably, despite the similar textural properties of Cu/HAP and βCD-Cu/HAP (see Table 2), βCD addition during synthesis exerted a noticeable impact on the crystalline structure and Cu dispersion. These findings indicate that βCD addition plays a

crucial role in modifying the structural aspects of the catalyst, which was also observed in previous studies [18–21].

Figure 2 illustrates the results of the H_2-TPR, which was employed to assess the Cu reducibility in the Cu-containing catalysts. The bare HAP support, consistent with previous studies [24,26], exhibited no noticeable H_2 consumption, indicating that all the H_2 consumption observed during catalyst characterization originated from the reduction of Cu species. The H_2-TPR profiles of the Cu-containing catalysts exhibit diverging characteristics in terms of the onset temperature of H_2 consumption (see Table S4). Specifically, the βCD-Cu/HAP catalyst lowered the onset temperature to ca. 80°C, as the Cu/HAP catalyst displayed an onset temperature of ca. 100°C. Furthermore, both Cu-containing catalysts exhibited four reduction peaks within the temperature range of 80 to 500 °C, denoted as peaks (I), (II), (III), and (IV).

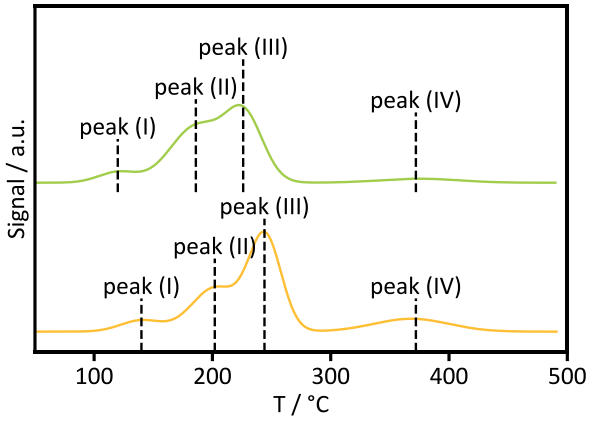

Figure 2: H_2-TPR profile of Cu/HAP ( ) and βCD-Cu/HAP ( ) catalysts.

Peak (I) could be correlated to the existence of the residual nitrate (NO_3^-) ions after calcination (detailed in SI; S3.2.). Peaks (II), (III), and (IV), which are associated with the reduction of CuO to Cu, can be categorized as surface Cu species (peaks (II) and (III)) and Cu doped into the lattice (peak (IV)) [24]. Peak (II) at temperatures of about 200 °C, is attributed to the reduction of surface highly dispersed Cu species. Peak (III), observed at temperatures ca. 250°C, is associated with the reduction of bulk CuO located on the catalyst surface [24,37,38]. In

comparison to the Cu/HAP catalyst, the reduction temperature of surface Cu species for βCD-Cu/HAP catalyst decreased by approximately 20 °C, implying the formation of smaller particles, consistent with N_2O chemisorption and XRD results (see Table 2). Finally, peak (IV), detected at temperatures above 370 °C, is indicative of Cu^{2+} ions incorporation into the lattice, resulting in the formation of hardly reducible Cu species [24,39].

Table 3 represents the TPR-H_2 profile peak deconvolution analysis (see Figure S5), which provides insights into the composition of Cu species in the catalysts. The analysis revealed that the contribution of surface highly dispersed Cu species amounted to 51.5% for βCD-Cu/HAP, whereas for Cu/HAP it was determined to be only 33.7%. Moreover, the contribution of bulk CuO and hardly reducible Cu species were observed to be noticeably lower for βCD-Cu/HAP compared to the Cu/HAP catalyst. Particularly, the contribution of hardly reducible Cu species was significantly reduced from 15.8 to 5.5%. These findings suggest that the βCD addition during synthesis impeded Cu particle agglomeration and doping of Cu^{2+} into the HAP lattice, ultimately promoting the formation of surface highly dispersed Cu species.

Table 3: Temperature ($T_{red,peak\#}$) and contribution (cont.) of H_2-TPR peaks corresponding to the reduction of CuO. Peak (II): surface highly dispersed Cu species, peak (II): bulk CuO (surface), and Peak (IV): hardly reducible Cu species (lattice).

Catalyst	Peak (II)		Peak (III)		Peak (IV)	
	$T_{red,II}$ $(°C)$	$Cont.$ $(\%)$	$T_{red,III}$ $(°C)$	$Cont.$ $(\%)$	$T_{red,IV}$ $(°C)$	$Cont.$ $(\%)$
Cu/HAP	202	33.7	244	50.5	368	15.8
βCD-Cu/HAP	186	51.5	226	43	374	5.5

Oxygen Storage Capacity (OSC) measurements provide valuable insights into the reoxidation capacity of a reduced catalyst. It has been previously reported [35] that OSC is directly proportional to the oxygen participating in the reaction, making it a reliable measure of the active sites concentration. No oxygen uptake was observed for the bare HAP support, within

the temperature range of 350 to 450 °C. The OSC for the Cu/HAP and βCD-Cu/HAP catalysts are presented in Figure 3a and exhibit a consistent linear increase within the temperature range. Moreover, the βCD-Cu/HAP catalyst showed an enhancement of at least 10% in OSC compared to Cu/HAP. However, it is worth mentioning that the OSC values for both catalysts have not reached the theoretical value determined by the ICP-OES method, as shown in Figure 3b. Specifically, the reoxidized Cu% at 450 °C amounted to ca. 72% and 80% for Cu/HAP and βCD-Cu/HAP catalysts, respectively.

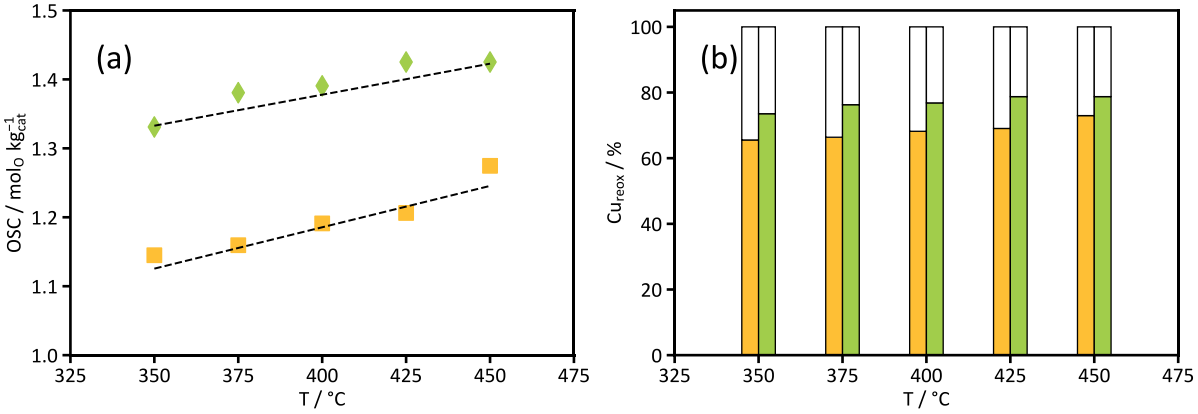

Figure 3: Evolution of the (a) OSC and (b) fraction of reoxidized Cu as a function of temperature for the Cu/HAP (,) and βCD-Cu/HAP (,) catalysts.

The observed increasing trend of OSC with temperature and remaining fraction of non-reoxidized Cu suggest the existence of two distinct types of active sites: easy-to-access and hard-to-access sites. This classification is further supported by the findings obtained from H_2-TPR as reported above. The easy-to-access sites correspond to the highly dispersed Cu species on the surface, which are near-surface oxygen sites and can be reoxidized at lower temperatures. Conversely, the hard-to-access sites correspond to the bulk CuO and Cu incorporated into the lattice, requiring higher temperatures for reoxidation. According to H_2-TPR results, both catalysts possessed large CuO particles and Cu incorporation into the HAP lattice, hindering the oxygen accessibility for reoxidation. This phenomenon provides an explanation for the existence of non-reoxidized Cu in both materials, even at the highest

295 temperature. Thus, the βCD-Cu/HAP catalyst exhibited a higher abundance of highly dispersed
296 Cu species (easy-to-access sites), consequently leading to a higher OSC and fraction of
297 reoxidized Cu.
298 XPS was carried out to gain insights into the oxidation states and relative composition at the
299 surface of the catalysts. Figure 4 depicts the Cu 2p spectra of the Cu-containing catalysts. The
300 binding energy of Cu $2p_{3/2}$ and $2p_{1/2}$ at 932.7 eV and 952.6 eV were observed for the Cu-
301 containing catalysts, respectively. The pronounced satellite peaks at 942 eV and 962 eV, a
302 distinctive characteristic of Cu^{2+}, along with the symmetry of the Cu $2p_{3/2}$ peaks, indicate the
303 presence of CuO in the Cu-containing catalysts [21,24]. The detailed deconvolution of the
304 Cu $2p_{3/2}$ peaks, coupled with an analysis of the Cu LMM Auger spectra, revealed no evidence
305 of additional Cu species, further confirming our findings of the Cu oxidation state.

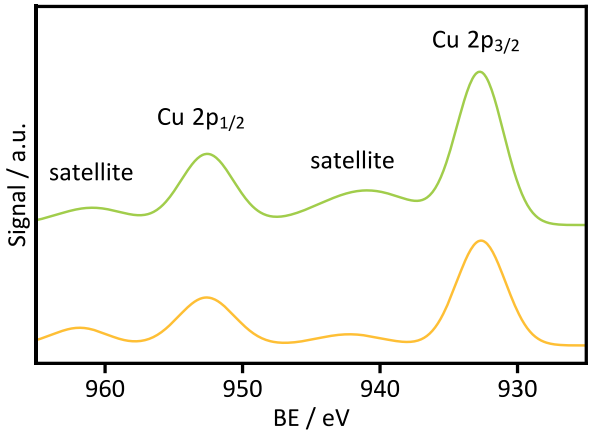

306
307 Figure 4: XPS spectra of Cu 2p and for the Cu/HAP ( ) and βCD-Cu/HAP ( ) catalysts.
308 The quantitative XPS analysis of surface chemical composition for the HAP, Cu/HAP and βCD-
309 Cu/HAP is presented in Table 4 (detailed in SI; S3.3. and Table S5). It is important to note the
310 considerable difference in the surface distribution of Cu and O atoms. The Cu/(Ca+P) ratio for
311 βCD-Cu/HAP was determined to be 0.12, whereas it was only 0.05 for Cu/HAP. This remarkable
312 increase in Cu presence at the surface is attributed to the βCD addition during synthesis, which
313 effectively improved the Cu dispersion on the catalyst surface. Furthermore, the O/Cu value

for the Cu/HAP sample was double that of βCD-Cu/HAP, possibly indicating surface segregation of a CuO phase. It has been previously reported [39,40] that larger particle sizes and higher Cu loading can increase the risk of surface segregation of Cu-containing phases. This phenomenon, in the case of Cu/HAP, leads to CuO segregating and forming larger particles, thereby concentrating the CuO in much smaller areas on the catalyst surface. As XPS only probes the surface, this segregation results in a significantly lower measured Cu concentration. Consistent with the XRD and N_2O chemisorption results presented in Table 2, the mean CuO crystallite size and Cu particle size for Cu/HAP were found to be significantly higher than that of βCD-Cu/HAP catalyst. Hence, Cu/HAP could be more prone to CuO segregation, which may render some CuO particles undetectable in XPS spectra. Our findings are consistent with previous studies [24,41], where it was observed that some CuO particles could not be detected as their size exceeded the penetration depth of the XPS (< 10 nm).

Table 4: Surface compositions calculated from the results obtained by XPS.

Material	Ca/P	Cu/(Ca+P)	O/Cu
HAP	1.51	-	-
Cu/HAP	1.62	0.05	30.8
βCD-Cu/HAP	1.42	0.12	14.7

3.2. Catalytic Activity

The catalytic tests include a thorough investigation of the impact of the reaction temperature and the CH_4 and O_2 inlet partial pressure on the performance of Cu/HAP and βCD-Cu/HAP catalysts, as a function of the space time. Additionally, a comparative analysis was carried out by analyzing the apparent activation energy and reaction orders determined via the initial reaction rate analysis for both catalysts. Finally, the TOF_0 value was employed as a comparative metric to assess the activity levels of the two considered catalysts.

It is worth outlining that the bare support (HAP) exhibited negligible conversion (<3%) even at the highest tested temperature of 450 °C. This could be attributed to the absence of any OSC (see Section 3.1), which serves as a reliable measure for the concentration of active sites for VOC total oxidation, hence, resulting in a lack of active sites on the catalyst surface to initiate the reaction. The low activity of HAP in CH_4 total oxidation has also been reported in a previous study [27], where HAP could not reach 4% conversion at 500 °C. Consequently, the bare support did not substantially contribute to the CH_4 conversion observed in the Cu-containing catalysts.

The impact of temperature and space time on the performance of Cu-containing catalysts was explored, as presented in Figure 5a and Figure 5b, respectively. Both catalysts exhibited an increasing trend in CH_4 conversion with rising temperature and space time. The βCD-Cu/HAP catalyst outperformed the Cu/HAP catalyst, exhibiting at least 1.2 to 2 times higher conversion as temperature and space time increased, respectively.

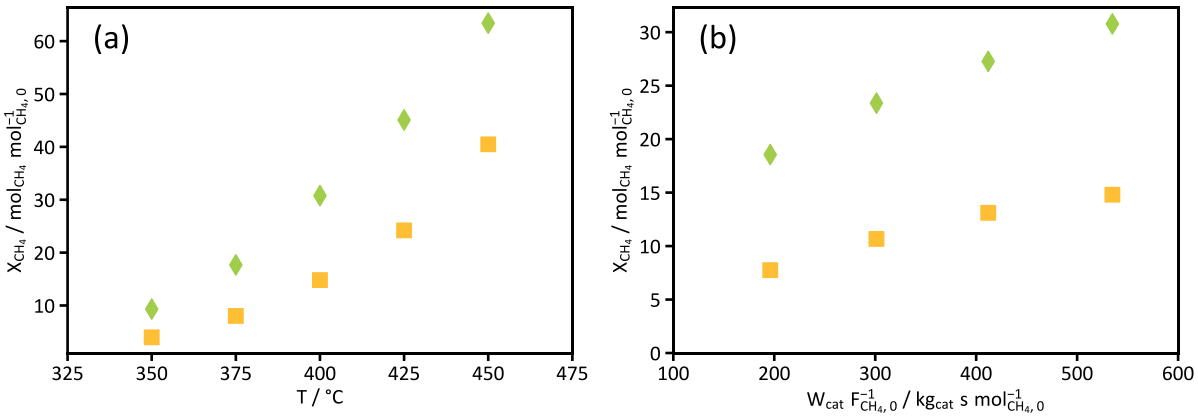

Figure 5: Effect of (a) temperature (space time = 535 kg_{cat} s $mol^{-1}_{CH_4}$) and (b) space time (T = 400 °C) on the performance of Cu/HAP (■) and βCD-Cu/HAP (♦) catalysts at initial CH_4 and O_2 partial pressure of 2.9 and 16.6 kPa, respectively.

The effect of the CH_4 and O_2 inlet partial pressure on the performance of Cu-containing catalysts was investigated, as presented in Figure 6a and Figure 6b, respectively. Figure 6 shows that an increasing inlet partial pressure of CH_4 and O_2 resulted in an increase in CH_4

conversion. The βCD-Cu/HAP catalyst exhibited at least 2 times higher CH_4 conversion compared to Cu/HAP catalyst for the same inlet partial pressure of the reactants.

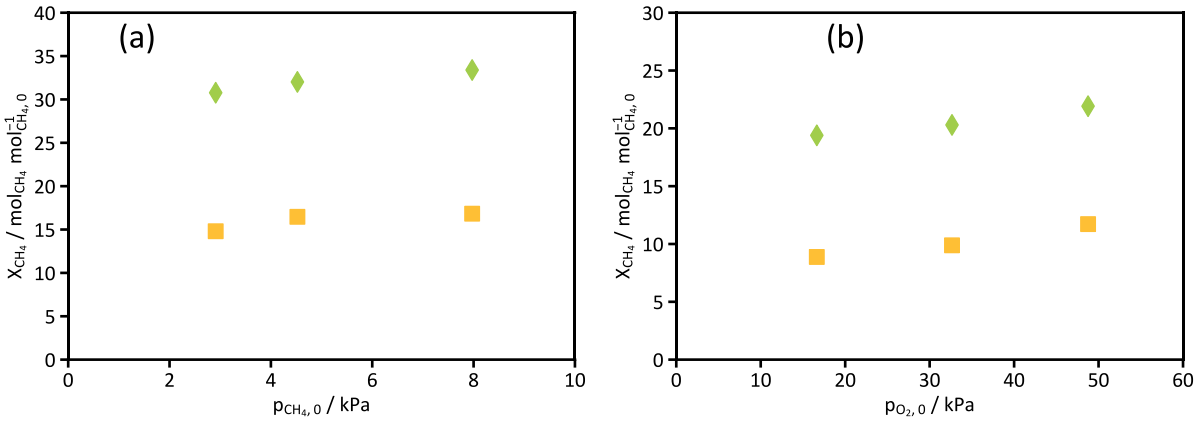

Figure 6: (a) Effect of CH_4 inlet partial pressure at $p_{O_2,0}$ = 16.6 kPa, T = 400 °C, space time = 196 kg_{cat} s $mol^{-1}_{CH_4}$; (b) Effect of O_2 inlet partial pressure at $p_{CH_4,0}$ = 2.91 kPa, T = 400 °C, space time = 535 kg_{cat} s $mol^{-1}_{CH_4}$ on the performance of Cu/HAP (■) and βCD-Cu/HAP (♦) catalysts.

A detailed initial rate analysis was carried out to compare the performance of Cu-containing catalysts. The initial reaction rates obtained via Eq. (S23) were employed to estimate reaction orders, apparent pre-exponential factors and activation energies, determined via Eq. (S26). The results are provided in Table 5. It should be noted that the CH_4 and O_2 reaction orders for both catalysts showed no significant temperature dependency. As expected, the estimated CH_4 and O_2 reaction orders were positive, signifying the positive role of the inlet partial pressures of both reactants, as observed in Figure 6. Interestingly, the catalysts exhibited a nearly constant CH_4 reaction order (ca. 0.62), whereas the O_2 reaction order amounted to 0.26 and 0.09 for Cu/HAP and βCD-Cu/HAP catalysts, respectively. This suggests that the CH_4 reaction order remained unaffected by variations in CuO particle size and Cu dispersion, while the O_2 reaction has been influenced by these factors. Moreover, the apparent activation energy of the βCD-Cu/HAP catalyst was 20 kJ mol^{-1} lower than that of Cu/HAP, which facilitated the CH_4 total oxidation when βCD was employed during synthesis. It is worth

outlining that the estimated apparent activation energies (78 and 96 kJ mol^{-1}, respectively) in this work are within the range (50 – 150 kJ mol^{-1}) of previously reported ones [11,42].

Table 5: Apparent CH_4 (m) and O_2 (n) reaction orders, pre-exponential factor $k_{0,app}$(mol kg_{cat}^{-1} $s^{-1}(kPa)^{-1+(m+n)}$), and activation energy $E_{a,app}$ (kJ mol^{-1}) obtained by Eq. (S26).

Catalyst	m	n	$k_{0,app}$	$E_{a,app}$
Cu/HAP	0.63 ± 0.06	0.26 ± 0.05	(3.32 ± 1.1) × 10^3	96 ± 2.6
βCD-Cu/HAP	0.62 ± 0.04	0.09 ± 0.03	(5.78 + 2.1) × 10^2	78 ± 1.6

The initial reaction rates obtained using Eq. (S23) were utilized to determine the TOF_0, see Eq. (S24). The obtained TOF_0 were used to conduct a thorough comparison of the catalytic performance of Cu/HAP and βCD-Cu/HAP (Figure 7). It was observed that the TOF_0 values for both catalysts exhibited an increasing trend as temperature was raised. In addition, the βCD-Cu/HAP catalyst exhibited substantially higher catalytic activity, approximately twofold, compared to the Cu/HAP catalyst across all examined temperatures. These findings are consistent with CH_4 conversion results evidenced in Figure 5 and Figure 6, where it was found that the CH_4 conversion for the βCD-Cu/HAP catalyst is significantly higher than that of Cu/HAP catalyst. Consequently, these results unequivocally demonstrate the enhanced catalytic performance of the βCD-Cu/HAP catalyst, attributed to the βCD addition during the synthesis procedure of Cu/HAP.

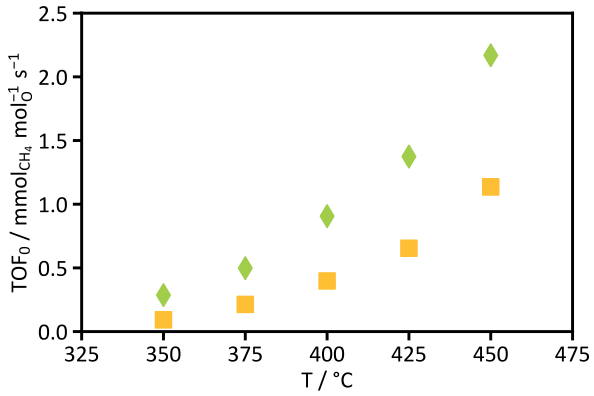

Figure 7: Evolution of TOF_0 as a function of temperature for Cu/HAP (■) and βCD-Cu/HAP (♦) catalysts at initial CH_4 and O_2 partial pressure of 2.9 and 16.6 kPa, respectively.

The addition of βCD during synthesis did not alter the fundamental reaction mechanism, as indicated by the constant CH_4 reaction order observed for both catalysts [43]. As previously discussed, the βCD addition during the synthesis of the βCD-Cu/HAP catalyst inhibited the interaction between Cu particles during the preparation, which effectively hindered Cu particle growth, resulting in the formation of smaller, well-dispersed CuO particles on its surface. These CuO particles exhibited enhanced reducibility and facilitated the redox processes. The latter was reflected in the increased OSC, indicating a greater capacity of the catalyst to store and release oxygen—crucial for efficiently refilling oxygen vacancies during the reaction. The enhanced OSC of the βCD-Cu/HAP catalyst underscored its superior ability to replenish oxygen vacancies more efficiently than its counterpart without βCD, ensuring an uninterrupted availability of active oxygen species for the CH_4 total oxidation. This continuous O_2 replenishment is fundamental to the catalyst's high level of activity, as it provides a continuous supply of O_2, critical for the CH_4 total oxidation reaction to proceed efficiently. The enhanced redox processes enabled a facile reaction of CH_4 with the available oxygen resources, i.e., CuO particles, making the reaction less dependent on gaseous O_2 for βCD-Cu/HAP. In addition, the low O_2 reaction order values for both catalysts (below 0.3) implies that the contribution of gaseous O_2 to the reaction is modest, as the zero reaction order for

O_2 may stem from the involvement of lattice oxygen in the reaction (MVK mechanism), whereas the unity reaction order for O_2 is typical for participation of adsorbed O_2 at low coverage (LH or ER mechanisms) [44]. However, a more detailed investigation of the reaction mechanism is conducted in Section 3.3, utilizing kinetic modeling that considers all potential mechanisms.

3.3. Model Selection

The well-dispersed βCD-Cu/HAP catalyst was chosen to investigate the reaction mechanism for CH_4 oxidation, due to its superior performance in comparison to the Cu/HAP catalyst. A comprehensive investigation was carried out across the experimental range outlined in Table *1*. In this section, a detailed examination of the preliminary model discrimination process is presented. Subsequently, the findings from non-isothermal regression and statistical and physico-chemical assessments are discussed, leading to the identification of the most appropriate (preferred) kinetic model that accurately describes the experimental data for CH_4 total oxidation over the βCD-Cu/HAP catalyst.

3.3.1. Preliminary Model Discrimination

A detailed initial rate analysis was carried out for Cu-containing catalysts, see section 3.2. The reaction orders of CH_4 and O_2 obtained for the βCD-Cu/HAP catalyst, presented in Table 5, and the effect of reaction products can be used to eliminate some kinetic models (detailed in SI; S3.4.). As a result, from the initial set of models (see Table S2), the LH models with the surface reaction as RDS and MVK, considering H_2O adsorption (on oxidized sites), stand out as the remaining relevant kinetic models for the total oxidation of CH_4 over the βCD-Cu/HAP catalyst. These models are detailed in Table 6 and will be further examined in the regression in Section 3.3.2.

Table 6: Remaining relevant kinetic models. For LH models, the surface reaction is RDS. For MVK models, $\gamma = 1 + K_{H_2O} p_{H_2O}$.

Model	Description	Rate equation
LH14	RDS: surface reaction molecular O_2 adsorption; 1 O_2; including H_2O	$r = k_r \frac{K_{CH_4} p_{CH_4} K_{O_2} p_{O_2}}{\left(1 + K_{CH_4} p_{CH_4} + K_{O_2} p_{O_2} + K_{H_2O} p_{H_2O}\right)^2}$
LH17	RDS: surface reaction molecular O_2 adsorption; 2 O_2; including H_2O	$r = k_r \frac{K_{CH_4} p_{CH_4} \left(K_{O_2} p_{O_2}\right)^2}{\left(1 + K_{CH_4} p_{CH_4} + K_{O_2} p_{O_2} + K_{H_2O} p_{H_2O}\right)^3}$
LH20	RDS: surface reaction dissociative O_2 adsorption; 1 O_2; including H_2O	$r = k_r \frac{K_{CH_4} p_{CH_4} \sqrt{K_{O_2} p_{O_2}}}{\left(1 + K_{CH_4} p_{CH_4} + \sqrt{K_{O_2} p_{O_2}} + K_{H_2O} p_{H_2O}\right)^2}$
LH23	RDS: surface reaction dissociative O_2 adsorption; 2 O_2; including H_2O	$r = k_r \frac{K_{CH_4} p_{CH_4} K_{O_2} p_{O_2}}{\left(1 + K_{CH_4} p_{CH_4} + \sqrt{K_{O_2} p_{O_2}} + K_{H_2O} p_{H_2O}\right)^3}$
MVK4	1 oxidized site; 1 reduced site; H_2O adsorption on oxidized sites	$r = \frac{k_{CH_4} p_{CH_4} k_{O_2} p_{O_2}}{2 k_{CH_4} p_{CH_4} + k_{O_2} p_{O_2} \gamma}$
MVK9	1 oxidized site; 2 reduced sites; H_2O adsorption on oxidized sites	$r = \frac{k_{CH_4} p_{CH_4}}{\gamma^2} \left(\gamma + \frac{k_{CH_4} p_{CH_4}}{k_{O_2} p_{O_2}} - \sqrt{2 \frac{k_{CH_4} p_{CH_4}}{k_{O_2} p_{O_2}} \gamma + \left(\frac{k_{CH_4} p_{CH_4}}{k_{O_2} p_{O_2}} \right)^2} \right)$
MVK14	2 oxidized sites; 1 reduced site; H_2O adsorption on oxidized sites	$r = \frac{k_{O_2} p_{O_2}}{2} \left(1 + \frac{k_{CH_4} p_{CH_4}}{4 k_{O_2} p_{O_2}} \gamma^2 - \gamma \sqrt{\frac{k_{CH_4} p_{CH_4}}{2 k_{O_2} p_{O_2}} + \left(\frac{k_{CH_4} p_{CH_4} \gamma}{4 k_{O_2} p_{O_2}} \right)^2} \right)$
MVK19	2 oxidized sites; 2 reduced sites; H_2O adsorption on oxidized sites	$r = \frac{k_{O_2} p_{O_2}}{2} \frac{1}{\left(1 + \gamma \sqrt{\frac{k_{O_2} p_{O_2}}{2 k_{CH_4} p_{CH_4}}} \right)^2}$

3.3.2. Parameter Estimation and Assessment of Model and Parameters

Following the preliminary model discrimination, a non-isothermal weighted regression analysis was carried out to identify the most adequate model among the remaining kinetic models listed in Table 6. The activation energies and adsorption enthalpies were directly estimated through regression analysis, while the corresponding pre-exponential factors and adsorption entropies were calculated based on the estimated parameters A' and $\Delta S'_{ads}$, using Eqs. (S29) and (S30). Furthermore, for each model, various regression performance metrics are provided, including the $WSSQ_{res}$, absolute value of maximum binary correlation coefficient, $F_{s,cal}$ and BIC.

3.3.2.1. LH models

The results of the weighted regression showed that all LH models were statistically significant. For all LH models, significant estimates were obtained for all parameters except for the activation energy (E_a) and CH_4 adsorption enthalpy (ΔH_{CH_4}). To alleviate strong correlation, the activation energy and pre-exponential factor were set to the values obtained from initial rate analysis (see Table 5). Subsequent regression with these adjustments revealed significant estimates for all models, but none satisfied the thermodynamic criteria completely. Consequently, all 4 LH models failed to provide meaningful thermodynamic properties and were thus excluded from further consideration in the discrimination of the kinetic model for the total oxidation of CH_4 over the βCD-Cu/HAP catalyst. More details are available in SI (S3.4.; Tables S13, S14, and S15).

3.3.2.2. MVK models

After the LH models could be eliminated, the MVK models (MVK4, 9, 14, and 19, see Table 6) were considered for evaluation. The results of non-isothermal parameter estimation for the MVK models are summarized in Table S16. All the MVK kinetic models were globally significant, with the corresponding parameters being statistically significant, as evidenced by the calculated *t* value exceeding the tabulated one. Furthermore, the thermodynamic constraints outlined in Eqs. (S42), (S43), and (S44) were satisfied for the considered MVK models. Notably, strong correlation ($\rho_{i,j} > 0.95$) was observed between A'_{CH_4} and $\Delta S'_{H_2O}$ in MVK4 and similarly, between $\Delta S'_{H_2O}$ and ΔH_{H_2O} in MVK9. Conversely, parameters were not highly correlated ($\rho_{i,j} < 0.95$) in MVK14 and MVK19. In addition, the estimated activation energy for the reduction reaction (E_{CH_4}) in MVK4 and MVK9 was approximately 30 kJ mol^{-1}. However, this value falls below the range of 50 – 150 kJ mol^{-1} [7,9,11,32,42,45], subsequently leading to the elimination of the MVK4 and MVk9 kinetic models from further consideration.

In contrast, MVK14 and MVK19 successfully estimated E_{CH_4} within the abovementioned range. The joint feature in these models is that they both involve two oxidized sites, with H_2O adsorption taking place on these oxidized sites. However, MVK14 and MVK19 are different in terms of the number of reduced sites, with MVK14 involving one, while MVK19 involving two reduced sites. Following a comprehensive statistical assessment, careful evaluation of activation energy and thermodynamic constraints, the MVK14 and MVK19 emerged both as reliable candidates. Consequently, the final model discrimination process was conducted between these two models. Despite both models yielding almost identical BIC values of ca. -6.2 (see Table S16), a key distinction was identified in the parameters related to the reoxidation reaction ($k_{O_2,0}$ and E_{O_2}). Given the difference in the reoxidation step, these models could exhibit different levels of dependency on gaseous O_2, leading to different partial reaction orders of O_2. Thus, a comparison of the partial reaction order of O_2 with the value obtained by initial rate analysis was employed to select the most appropriate kinetic model among MVK14 and MVK19. The O_2 partial reaction order was determined using Eq. (S41), resulting in a value of 0.07 for MVK14 and 0.22 for MVK19. The O_2 reaction order obtained through initial rate analysis of the experimental data (see Table 5) was 0.09, demonstrating that MVK14 predicts the O_2 partial reaction order more accurately. Therefore, the MVK14 kinetic model was deemed the "preferred" kinetic model among all the proposed models, demonstrating its suitability for accurately explaining the experimental data for CH_4 total oxidation over βCD-Cu/HAP catalyst.

The final results of the non-isothermal regression for MVK14 are presented in Table 7 (see Figure S7 in SI for isothermal regression results). For comparative analysis, this model was applied to the experimental data of Cu/HAP catalyst, with these results also presented in Table 7. The results revealed a substantial decrease (0.5 X) in the E_{CH_4} for the βCD-Cu/HAP catalyst,

likely due to its enhanced reducibility. Additionally, the ΔH_{H_2O} was found to be significantly higher (4 X), indicating stronger interactions between H_2O molecules and oxidized sites. This strong interaction can be attributed to the abundant oxidized sites on the surface of the βCD-Cu/HAP catalyst, providing sufficient adsorption sites for H_2O. Conversely, the Cu/HAP catalyst exhibited weaker interactions between H_2O and oxidized sites, likely stemming from the limited availability of oxidized sites. This limitation is attributed to the catalyst's lower Cu dispersion and the high competition between CH_4 and H_2O for the available oxidized sites. Furthermore, the regression results for βCD-Cu/HAP catalyst revealed that the reoxidation pre-exponential factor value was considerably higher than that of the reduction step. Additionally, the activation energies associated with reduction (E_{CH_4}) and reoxidation (E_{O_2}) were ca. 60 and 93 kJ mol^{-1}, respectively. These values are consistent with previously reported findings for CH_4 total oxidation using the MVK mechanism (detailed in SI; S3.6.).

Table 7: Kinetic parameter results for the MVK14 model for Cu/HAP and βCD-Cu/HAP catalysts.

parameter	unit	MVK14 (Cu/HAP)	MVK14 (βCD-Cu/HAP)
$k_{CH_4,0}$	/ mol $kg_{cat}^{-1}s^{-1}kPa^{-1}$	3.9×10^5	35.9
E_{CH_4}	/ kJ mol^{-1}	118.72 ± 25.1	59.9 ± 8.7
$k_{O_2,0}$	/ mol $kg_{cat}^{-1}s^{-1}kPa^{-1}$	1129.2	15325.2
E_{O_2}	/ kJ mol^{-1}	84.39 ± 67.9	93.4 ± 22.0
ΔS_{H_2O}	/ J mol^{-1}K^{-1}	-42.9	-168.3
$-\Delta H_{H_2O}$	/ kJ mol^{-1}	26.3 ± 20.22	110.7 ± 9.3

Figure 8a depicts the parity diagram for model MVK14, revealing an outstanding agreement with the corresponding experimental values, wherein both training and validation datasets were reproduced within a 10% deviation. Furthermore, Figure 8b-d presents the capability of

MVK14 for describing the experimental data as a function of operating conditions, including temperature, space time, and inlet partial pressure of CH_4 and O_2. The model exhibited an excellent agreement with experimental data, effectively capturing the effect of variations in operating conditions on CH_4 conversion.

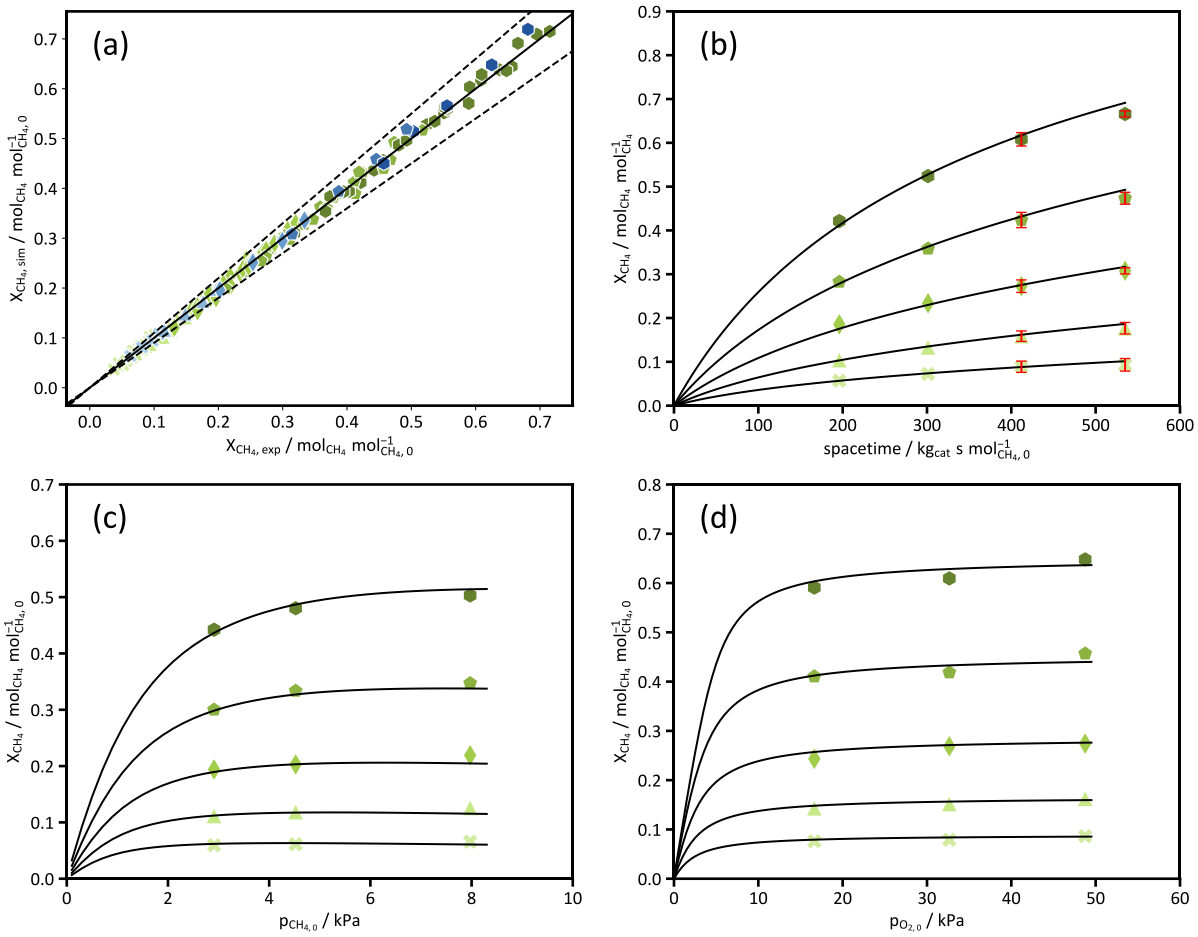

Figure 8: (a) Parity plot including both training (green) and validation datasets (blue). CH_4 conversion (b) as a function of $W_{cat}\ F^{-1}_{CH_4,0}$ at $p_{CH_4,0}$= 2.9 kPa and $p_{O_2,0}$= 16.9 kPa, (c) as a function of $p_{CH_4,0}$ at $p_{O_2,0}$= 32.6 kPa, $W_{cat}\ F^{-1}_{CH_4,0}$= 196 kg_{cat} s $mol^{-1}_{CH_4,0}$, and (d) as a function of $p_{O_2,0}$ at $p_{CH_4,0}$= 4.52 kPa, $W_{cat}\ F^{-1}_{CH_4,0}$= 344 kg_{cat} s $mol^{-1}_{CH_4,0}$. Experimental data were obtained at T= 350 °C (✖), 375 °C (▲), 400 °C (♦), 425 °C (⬟), and 450 °C (⬢) using βCD-Cu/HAP catalyst. Validation datasets were obtained at $p_{CH_4,0}$= 3.1 kPa, $p_{O_2,0}$= 45.7 kPa, $W_{cat}\ F^{-1}_{CH_4,0}$= 96 – 535 kg_{cat} s $mol^{-1}_{CH_4,0}$, T= 350 °C (✖), 375 °C (▲), 400 °C (♦), 425 °C (⬟), and 450 °C (⬢). The dashed lines in the parity plot display the 10% deviation. Full lines were obtained with the MVK14 model (preferred model). The dashed lines in the parity plot display the 10% deviation. Full lines were obtained with the MVK14 model (preferred model).

The normal probability plot presented in Figure S8 highlights the normal distribution of weighted residuals, given their close adherence to a linear trend with an R^2 value exceeding 0.99. Additionally, the weighted residuals are plotted (Figure S8) against the experimental values and operating conditions which consistently reveal the absence of any systematic correlation between weighted residuals and the operating conditions. The weighted residuals are uniformly distributed across horizontal axis, indicating that mean value of weighted residual is zero.

The same set of diagrams – parity, performance, normal probability, and residual – were also plotted using data from the Cu/HAP catalyst, as seen in Figures S9 and S10. These figures reveal no significant discrepancies when compared to the plots for the βCD-Cu/HAP catalyst, indicating a consistent modeling performance across both catalysts.

The MVK14 successfully met all the criteria upon thorough statistical and physico-chemical assessments. This preferred model proposes that CH_4 total oxidation over βCD-Cu/HAP catalyst follows the MVK mechanism. This is in accordance with the experimentally obtained low value (0.09) for the reaction order of O_2, suggesting the participation of surface lattice oxygen in the reaction, as explained in Section 3.2. Furthermore, the MVK 14 rate equation (see Eq. S14) demonstrates a critical dependence on the square of oxidized sites' surface coverage (θ_{ox}^2) and a direct proportionality to the coverage of reduced sites (θ), signifying the essential role of oxidized sites in CH_4 total oxidation. Additionally, the model incorporated surface coverage of H_2O (see Eqs. S17 and S18), elucidating the adverse impact of H_2O on the availability of oxidized sites and, consequently, on the reaction kinetics. The MVK mechanism has also been proposed for CH_4 total oxidation over various catalysts including Pd-based [10,46], Cu-based [31], and perovskite [9]. Given that the reaction temperature was above 350 °C in this work, the adsorption of CH_4 at such temperatures is negligible [47]. This implies that

544 CH_4 is involved in a chemisorption with the catalyst surface (surface lattice oxygen), further
545 supporting the applicability of the MVK mechanism.
546 The initial step in the MVK mechanism is reduction, where CH_4 reduces oxidized sites and
547 generates an oxygen vacancy. It should be noted that CH_4 is the most stable hydrocarbon due
548 to its symmetric tetrahedral structure, consisting of four equivalent C-H bonds [7]. This high
549 stability likely necessitated the involvement of two surface lattice oxygen in the reduction step
550 (two oxidized sites $[O]^*$, see steps 17 and 18 in Table S1). Subsequently, CH_4 dissociated into
551 intermediate species which are much more active than CH_4 [48]. These intermediates oxidized
552 into CO_2 and H_2O, both of which desorb readily. Then, the produced H_2O adsorbed on the
553 oxidized sites, thereby initiating a competition with CH_4. This competition between CH_4 and
554 H_2O for adsorption on oxidized sites reduces the availability of active sites, consequently
555 diminishing the reaction rate, which explains the strong inhibition effect of H_2O, as discussed
556 in Section 3.3.1.
557 The oxygen vacancy generated during the reduction step was replenished by gaseous O_2 as
558 well as the migration of the bulk lattice oxygen via diffusion [49]. As discussed in Section 3.2,
559 the reaction rate exhibited limited dependence on gaseous O_2. Consequently, it may mainly
560 be the diffusion of bulk lattice oxygen with little contribution of gaseous O_2 that served to
561 replenish the oxygen vacancies. This diffusion process was likely rapid enough [47,49,50] to
562 facilitate the swift reoxidation of the catalyst. As a result, the catalyst dependency on gaseous
563 O_2 decreased, allowing for facile reduction and reoxidation via mainly bulk lattice diffusion,
564 with gaseous O_2 playing a minor role.
565 The visual representation of the CH_4 total oxidation mechanism over the βCD-Cu/HAP catalyst
566 is represented in Figure *9*. This reaction mechanism proceeded via the following steps. Initially,
567 in the absence of H_2O in the gas phase, CH_4 reduced the catalyst surface utilizing two oxidized

sites and produced H_2O and CO_2, which desorbed rapidly (Figure 9a). Subsequently, the produced H_2O adsorbed on the oxidized sites, thereby initiating a competition with CH_4, which explains the strong inhibition effect of H_2O. Then, rapid diffusion of bulk lattice oxygen to the surface with the assistance of the gaseous O_2 via involving one reduced site, replenished the oxygen vacancies (Figure 9b). This enabled the reaction to proceed through a repetitive cycle of reduction in the presence of H_2O (Figure 9c) followed by reoxidation (Figure 9b).

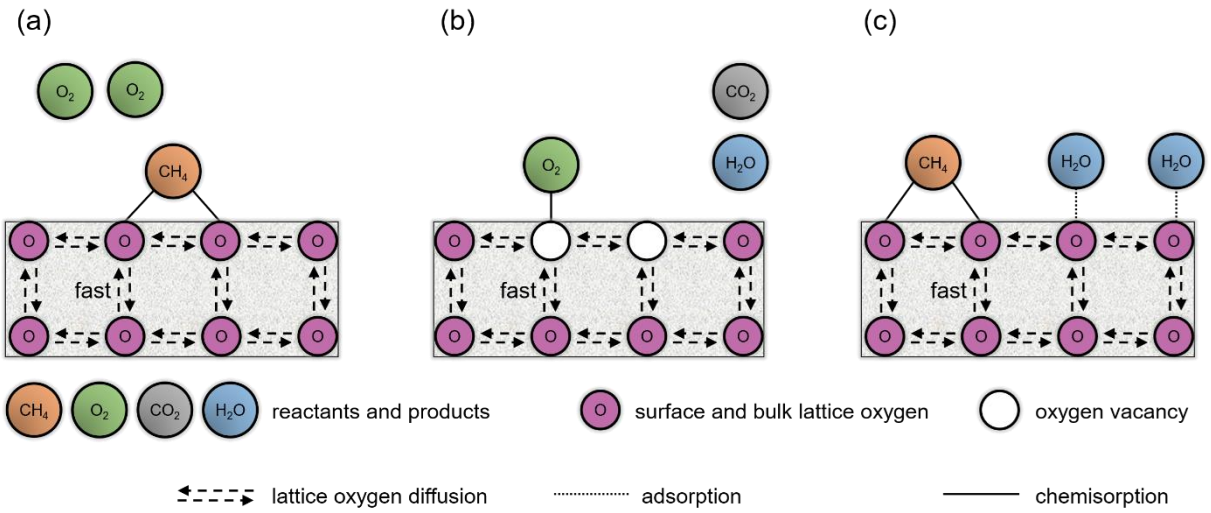

Figure 9: The proposed mechanism of CH_4 total oxidation over βCD-Cu/HAP catalyst; (a) reduction step at the start of the reaction; (b) reoxidation step; and (c) reduction step in the presence of H_2O.

Although the MVK14 model accurately predicted the experimental data for CH_4 total oxidation over the βCD-Cu/HAP catalyst, a slight discrepancy was observed at higher space times, hinting at a potential inhibitory effect of H_2O as it competes with CH_4 for oxidized sites. This discrepancy may stem from the mean-field nature of the model, which simplifies complex interactions by averaging behavior over the entire experimental domain. To address these nuances and better understand H_2O impact, integrating molecular modeling into future work is recommended. Additionally, to counteract the inhibitory effect of H_2O, future research could explore enhancing the hydrophobicity of support materials and optimizing operational conditions to balance CH_4 adsorption and H_2O desorption effectively. Such initiatives broaden

our understanding of the H_2O impact, offering avenues for improving catalyst design and performance.

4. Conclusion

The βCD addition during the synthesis procedure led to smaller Cu particles on the βCD-Cu/HAP catalyst and, hence, enhanced Cu dispersion, compared to the Cu/HAP catalyst. This enhancement in dispersion led to a significantly improvement of redox properties, allowing reduction at lower temperatures and facile reoxidation, which in turn increased OSC. These improvements enabled more facile reactions of CH_4 with CuO particles on the βCD-Cu/HAP catalyst, making the reaction less dependent on gaseous O_2. These distinctive characteristics of the βCD-Cu/HAP catalyst contributed to its superior catalytic activity (twofold) compared to Cu/HAP for CH_4 total oxidation.

According to the kinetic model selection procedure, the CH_4 total oxidation follows an MVK mechanism involving two oxidized sites, one reduced site, and H_2O adsorption on oxidized sites. The predominant mechanism for replenishing oxygen vacancies in the catalyst appears to be the fast diffusion of bulk lattice oxygen, with a limited contribution from gaseous O_2. Additionally, the H_2O adsorption on oxidized sites creates competition with CH_4, explaining the pronounced inhibition effect of H_2O observed in experimental data.

Acknowledgments

This work was performed in the framework of a Concerted Research Action (GOA, grant number 01G00319), financed by Ghent University. We would like to acknowledge the INSTALAB core facility at Ghent University for providing us with their analytical service and granting access to their instrumental equipment.

Appendix A. Supporting information

Supplementary material related to this article are provided in a separate document.

Declaration of Generative AI and AI-assisted Technologies in the Writing Process

During the preparation of this work, the author(s) used ChatGPT 3.5 in order to improve readability and language but not to interpret data or draw scientific conclusions. After using this tool, the author(s) reviewed and edited the content as needed and take(s) full responsibility for the content of the publication.

References

[1] H. Gu, J. Lan, H. Hu, F. Jia, Z. Ai, L. Zhang, X. Liu, Surface oxygen vacancy-dependent molecular oxygen activation for propane combustion over α-MnO_2, J Hazard Mater. 460 (2023). https://doi.org/10.1016/j.jhazmat.2023.132499.

[2] C. He, J. Cheng, X. Zhang, M. Douthwaite, S. Pattisson, Z. Hao, Recent Advances in the Catalytic Oxidation of Volatile Organic Compounds: A Review Based on Pollutant Sorts and Sources, Chem Rev. 119 (2019) 4471–4568. https://doi.org/10.1021/acs.chemrev.8b00408.

[3] L. Sun, X. Liang, H. Liu, H. Cao, X. Liu, Y. Jin, X. Li, S. Chen, X. Wu, Activation of Co-O bond in (110) facet exposed Co_3O_4 by Cu doping for the boost of propane catalytic oxidation, J Hazard Mater. 452 (2023). https://doi.org/10.1016/j.jhazmat.2023.131319.

[4] X. Feng, F. Luo, Y. Chen, D. Lin, Y. Luo, L. Xiao, X. Liu, X. Sun, Q. Qian, Q. Chen, Boosting total oxidation of propane over CeO_2@Co_3O_4 nanofiber catalysts prepared by multifluidic coaxial electrospinning with continuous grain boundary and fast lattice oxygen mobility, J Hazard Mater. 406 (2021). https://doi.org/10.1016/j.jhazmat.2020.124695.

[5] Z. Zakaria, S.K. Kamarudin, Direct conversion technologies of methane to methanol: An overview, Renewable and Sustainable Energy Reviews. 65 (2016) 250–261. https://doi.org/10.1016/j.rser.2016.05.082.

[6] L.S. Escandón, S. Ordóñez, A. Vega, F. V. Díez, Sulphur poisoning of palladium catalysts used for methane combustion: Effect of the support, J Hazard Mater. 153 (2008) 742–750. https://doi.org/10.1016/j.jhazmat.2007.09.017.

639 [7] M. Stoian, V. Rogé, L. Lazar, T. Maurer, J.C. Védrine, I.C. Marcu, I. Fechete, Total
640 oxidation of methane on oxide and mixed oxide ceria-containing catalysts, Catalysts. 11
641 (2021) 1–42. https://doi.org/10.3390/catal11040427.
642 [8] J. Dou, Y. Tang, L. Nie, C.M. Andolina, X. Zhang, S. House, Y. Li, J. Yang, F. (Feng) Tao,
643 Complete Oxidation of Methane on Co_3O_4/CeO_2 Nanocomposite: A Synergic Effect,
644 Catal Today. 311 (2018) 48–55. https://doi.org/10.1016/j.cattod.2017.12.027.
645 [9] R. Auer, F.C. Thyrion, Kinetics of the total oxidation of methane over a $La_{0.9}Ce_{0.1}CoO_3$
646 perovskite catalyst, Ind Eng Chem Res. 41 (2002) 680–690.
647 https://doi.org/10.1021/ie0104924.
648 [10] P. Hurtado, S. Ordóñez, H. Sastre, F. V. Díez, Development of a kinetic model for the
649 oxidation of methane over Pd/Al_2O_3 at dry and wet conditions, Appl Catal B. 51 (2004)
650 229–238. https://doi.org/10.1016/j.apcatb.2004.03.006.
651 [11] G. Águila, F. Gracia, J. Cortés, P. Araya, Effect of copper species and the presence of
652 reaction products on the activity of methane oxidation on supported CuO catalysts,
653 Appl Catal B. 77 (2008) 325–338. https://doi.org/10.1016/j.apcatb.2007.08.002.
654 [12] P.W. Park, J.S. Ledford, The influence of surface structure on the catalytic activity of
655 alumina supported copper oxide catalysts. Oxidation of carbon monoxide and methane,
656 Appl Catal B. 15 (1998) 221–231. https://doi.org/10.1016/S0926-3373(98)80008-8.
657 [13] M. Konsolakis, S.A.C. Carabineiro, P.B. Tavares, J.L. Figueiredo, Redox properties and
658 VOC oxidation activity of Cu catalysts supported on $Ce_{1-x}Sm_xO_\delta$ mixed oxides, J Hazard
659 Mater. 261 (2013) 512–521. https://doi.org/10.1016/j.jhazmat.2013.08.016.
660 [14] P. Xin-yu, L.I.U. Li-jun, S. Bo-xiong, B. Yao, S.U. Li-chao, Insight into the catalytic
661 oxidation of toluene over M / ZSM-5 (M = Cu , Mn , Fe , Ce , Ti) catalysts, Journal of

662 Fuel Chemistry and Technology. 51 (2023) 841–851. https://doi.org/10.1016/S1872-
663 5813(22)60069-0.
664 [15] L. Kundakovic, M. Flytzani-Stephanopoulos, Reduction characteristics of copper oxide
665 in cerium and zirconium oxide systems, Appl Catal A Gen. 171 (1998) 13–29.
666 https://doi.org/10.1016/S0926-860X(98)00056-8.
667 [16] Y. Chen, Y. Liu, D. Mao, J. Yu, Y. Zheng, X. Guo, Z. Ma, Facile cyclodextrin-assisted
668 synthesis of highly active CuO-CeO_2/MCF catalyst for CO oxidation, J Taiwan Inst Chem
669 Eng. 113 (2020) 16–26. https://doi.org/10.1016/j.jtice.2020.07.015.
670 [17] H. Liu, Y. Li, H. Wu, T. Miyake, D. He, CO2 reforming of methane over Ni/SBA-15
671 prepared with β-cyclodextrin - Role of β-cyclodextrin in Ni dispersion and performance,
672 Int J Hydrogen Energy. 38 (2013) 15200–15209.
673 https://doi.org/10.1016/j.ijhydene.2013.09.095.
674 [18] L. Bai, F. Wyrwalski, J.F. Lamonier, A.Y. Khodakov, E. Monflier, A. Ponchel, Effects of β-
675 cyclodextrin introduction to zirconia supported-cobalt oxide catalysts: From molecule-
676 ion associations to complete oxidation of formaldehyde, Appl Catal B. 138–139 (2013)
677 381–390. https://doi.org/10.1016/j.apcatb.2013.03.015.
678 [19] L. Bai, F. Wyrwalski, M. Safariamin, R. Bleta, J.F. Lamonier, C. Przybylski, E. Monflier, A.
679 Ponchel, Cyclodextrin-cobalt (II) molecule-ion pairs as precursors to active Co_3O_4/ZrO_2
680 catalysts for the complete oxidation of formaldehyde: Influence of the cobalt source, J
681 Catal. 341 (2016) 191–204. https://doi.org/10.1016/j.jcat.2016.07.006.
682 [20] M. Ibrahim, M. Labaki, A. Ponchel, J.M. Giraudon, O. Gardoll, J.F. Lamonier, Beneficial
683 Effect of β-Cyclodextrin Assisted Synthesis of CuO/Hydroxyapatite Catalyst in Toluene
684 Oxidation, ChemCatChem. 15 (2023). https://doi.org/10.1002/cctc.202200943.

[21] C. Wang, Y. Li, H. Liu, Z. Hu, X. Hao, H. Jia, J. Chen, C. Lu, Constructing a high concentration CuO/CeO_2 interface for complete oxidation of toluene: The fantastic application of spatial confinement strategy, Journal of Rare Earths. 41 (2023) 850–861. https://doi.org/10.1016/j.jre.2023.01.001.

[22] K. Okumura, T. Kobayashi, H. Tanaka, M. Niwa, Toluene combustion over palladium supported on various metal oxide supports, Appl Catal B. 44 (2003) 325–331. https://doi.org/10.1016/S0926-3373(03)00101-2.

[23] D. Chlala, J.M. Giraudon, N. Nuns, C. Lancelot, R.N. Vannier, M. Labaki, J.F. Lamonier, Active Mn species well dispersed on Ca^{2+} enriched apatite for total oxidation of toluene, Appl Catal B. 184 (2016) 87–95. https://doi.org/10.1016/j.apcatb.2015.11.020.

[24] Z. Qu, Y. Sun, D. Chen, Y. Wang, Possible sites of copper located on hydroxyapatite structure and the identification of active sites for formaldehyde oxidation, J Mol Catal A Chem. 393 (2014) 182–190. https://doi.org/10.1016/j.molcata.2014.06.008.

[25] R.K. More, N.R. Lavande, P.M. More, Copper supported on Co substituted hydroxyapatite for complete oxidation of diesel engine exhaust and VOC, Molecular Catalysis. 474 (2019) 110414. https://doi.org/10.1016/j.mcat.2019.110414.

[26] M. Ibrahim, M. Labaki, N. Nuns, J.M. Giraudon, J.F. Lamonier, Cu−Mn Hydroxyapatite Materials for Toluene Total Oxidation, ChemCatChem. 12 (2020) 550–560. https://doi.org/10.1002/cctc.201901336.

[27] Z. Boukha, B. de Rivas, J.R. González-Velasco, J.I. Gutiérrez-Ortiz, R. López-Fonseca, Comparative study of the efficiency of different noble metals supported on hydroxyapatite in the catalytic lean methane oxidation under realistic conditions, Materials. 14 (2021). https://doi.org/10.3390/ma14133612.

[28] Z. Boukha, A. Choya, M. Cortés-Reyes, B. de Rivas, L.J. Alemany, J.R. González-Velasco, J.I. Gutiérrez-Ortiz, R. López-Fonseca, Influence of the calcination temperature on the activity of hydroxyapatite-supported palladium catalyst in the methane oxidation reaction, Appl Catal B. 277 (2020) 119280. https://doi.org/10.1016/j.apcatb.2020.119280.

[29] L. He, Y. Fan, J. Bellettre, J. Yue, L. Luo, A review on catalytic methane combustion at low temperatures: Catalysts, mechanisms, reaction conditions and reactor designs, Renewable and Sustainable Energy Reviews. 119 (2020). https://doi.org/10.1016/j.rser.2019.109589.

[30] C.Y. Lin, F.C. Chou, D.H. Tsai, Mechanistic understanding of surface reduction of Cu–Ce–O hybrid nanoparticles for catalytic methane combustion, J Taiwan Inst Chem Eng. 92 (2018) 80–90. https://doi.org/10.1016/j.jtice.2018.01.049.

[31] Y. Feng, P.M. Rao, D.R. Kim, X. Zheng, Methane oxidation over catalytic copper oxides nanowires, Proceedings of the Combustion Institute. 33 (2011) 3169–3175. https://doi.org/10.1016/j.proci.2010.05.017.

[32] J.W. Veldsink, G.F. Versteeg, W.P.M. van Swaaij, Intrinsic kinetics of the oxidation of methane over an industrial copper(II) oxide catalyst on a γ-alumina support, The Chemical Engineering Journal and The Biochemical Engineering Journal. 57 (1995) 273–283. https://doi.org/10.1016/0923-0467(94)02872-8.

[33] K. Van der Borght, K. Toch, V. V. Galvita, J.W. Thybaut, G.B. Marin, Information-driven catalyst design based on high-throughput intrinsic kinetics, Catalysts. 5 (2015) 1948–1968. https://doi.org/10.3390/catal5041948.

[34] R.J. Berger, E.H. Stitt, G.B. Marin, F. Kapteijn, J.A. Moulijn, Chemical reaction kinetics in practice, Cattech. 5 (2001) 30–60.

[35] P.M. Heynderickx, J.W. Thybaut, H. Poelman, D. Poelman, G.B. Marin, Kinetic modeling of the total oxidation of propane over anatase and vanadia sputter deposited catalysts, Appl Catal B. 90 (2009) 295–306. https://doi.org/10.1016/j.apcatb.2009.03.020.

[36] S. Karnjanakom, G. Guan, B. Asep, X. Hao, S. Kongparakul, C. Samart, A. Abudula, Catalytic Upgrading of Bio-Oil over Cu/MCM-41 and Cu/KIT-6 Prepared by β-Cyclodextrin-Assisted Coimpregnation Method, Journal of Physical Chemistry C. 120 (2016) 3396–3407. https://doi.org/10.1021/acs.jpcc.5b11840.

[37] B. Putrakumar, P.K. Seelam, G. Srinivasarao, K. Rajan, R. Rajesh, K. Ramachandra Rao, T. Liang, High performance and sustainable copper-modified hydroxyapatite catalysts for catalytic transfer hydrogenation of furfural, Catalysts. 10 (2020) 1–17. https://doi.org/10.3390/catal10091045.

[38] H. Tounsi, S. Djemal, C. Petitto, G. Delahay, Copper loaded hydroxyapatite catalyst for selective catalytic reduction of nitric oxide with ammonia, Appl Catal B. 107 (2011) 158–163. https://doi.org/10.1016/j.apcatb.2011.07.009.

[39] Z. Boukha, J.L. Ayastuy, M. Cortés-Reyes, L.J. Alemany, J.R. González-Velasco, M.A. Gutiérrez-Ortiz, Catalytic performance of Cu/hydroxyapatite catalysts in CO preferential oxidation in H_2 -rich stream, Int J Hydrogen Energy. 44 (2019) 12649–12660. https://doi.org/10.1016/j.ijhydene.2018.12.157.

[40] J. Tang, L. Deng, S. Xiao, H. Deng, X. Zhang, W. Hu, Chemical Ordering and Surface Segregation in Cu-Pt Nanoalloys: The Synergetic Roles in the Formation of Multishell Structures, Journal of Physical Chemistry C. 119 (2015) 21515–21527. https://doi.org/10.1021/acs.jpcc.5b06145.

754 [41] D. Chlala, J.M. Giraudon, N. Nuns, M. Labaki, J.F. Lamonier, Highly Active Noble-Metal-
755 Free Copper Hydroxyapatite Catalysts for the Total Oxidation of Toluene,
756 ChemCatChem. 9 (2017) 2275–2283. https://doi.org/10.1002/cctc.201601714.
757 [42] J. Chen, B.D. Carlson, T.J. Toops, Z. Li, M.J. Lance, S.G. Karakalos, J.S. Choi, E.A.
758 Kyriakidou, Methane Combustion Over Ni/$Ce_xZr_{1-x}O_2$ Catalysts: Impact of Ceria/Zirconia
759 Ratio, ChemCatChem. 12 (2020) 5558–5568. https://doi.org/10.1002/cctc.202000947.
760 [43] T.F. Garetto, C.R. Apesteguía, Oxidative catalytic removal of hydrocarbons over Pt/Al_2O_3
761 catalysts, Catal Today. 62 (2000) 189–199. https://doi.org/10.1016/S0920-
762 5861(00)00420-X.
763 [44] H. Arai, T. Yamada, K. Eguchi, T. Seiyama, Catalytic combustion of methane over various
764 perovskite-type oxides, Appl Catal. 26 (1986) 265–276. https://doi.org/10.1016/S0166-
765 9834(00)82556-7.
766 [45] V.C. Belessi, A.K. Ladavos, G.S. Armatas, P.J. Pomonis, Kinetics of methane oxidation
767 over La-Sr-Ce-Fe-O mixed oxide solids, Physical Chemistry Chemical Physics. 3 (2001)
768 3856–3862. https://doi.org/10.1039/b103426j.
769 [46] P. Stefanov, S. Todorova, A. Naydenov, B. Tzaneva, H. Kolev, G. Atanasova, D.
770 Stoyanova, Y. Karakirova, K. Aleksieva, On the development of active and stable Pd-
771 Co/γ-Al_2O_3 catalyst for complete oxidation of methane, Chemical Engineering Journal.
772 266 (2015) 329–338. https://doi.org/10.1016/j.cej.2014.12.099.
773 [47] F. Teng, W. Han, S. Liang, B. Gaugeu, R. Zong, Y. Zhu, Catalytic behavior of
774 hydrothermally synthesized $La_{0.5}Sr_{0.5}MnO_3$ single-crystal cubes in the oxidation of CO
775 and CH_4, J Catal. 250 (2007) 1–11. https://doi.org/10.1016/j.jcat.2007.05.007.
776 [48] C. Liu, H. Xian, Z. Jiang, L. Wang, J. Zhang, L. Zheng, Y. Tan, X. Li, Insight into the
777 improvement effect of the Ce doping into the SnO_2 catalyst for the catalytic combustion

of methane, Appl Catal B. 176–177 (2015) 542–552. https://doi.org/10.1016/j.apcatb.2015.04.042.

[49] J. Zhu, J.G. Van Ommen, H.J.M. Bouwmeester, L. Lefferts, Activation of O_2 and CH_4 on yttrium-stabilized zirconia for the partial oxidation of methane to synthesis gas, J Catal. 233 (2005) 434–441. https://doi.org/10.1016/j.jcat.2005.05.012.

[50] V. Balcaen, R. Roelant, H. Poelman, D. Poelman, G.B. Marin, TAP study on the active oxygen species in the total oxidation of propane over a $CuO\text{-}CeO_2/\gamma\text{-}Al_2O_3$ catalyst, Catal Today. 157 (2010) 49–54. https://doi.org/10.1016/j.cattod.2010.02.048.